Parity–time-symmetric whispering-gallery microcavities

A1. Fabrication of Erbium-doped silica microtoroid. The PT-symmetric optical resonator system investigated here is formed by two coupled WGM microtoroids. The passive (lossy) microtoroid is made from silica[1], whereas the active (with gain) resonator is made from erbium-ion-doped silica film, which is formed using sol-gel synthesis[2,3]. The flow chart for the preparation of the sol-gel silica film is as follows (**Fig. S1**):

1) Sol-gel precursor solution is prepared by mixing tetraethoxysilane (TEOS) in isopropanol alcohol (IPA), water (H_2O), and hydrochloric acid (HCl). The weight ratio of TEOS:IPA:H_2O:HCl is 0.6:6.5:0.7:6.1.

2) Erbium ions are incorporated by adding erbium nitrate $Er(NO_3)_3$ to the precursor solution at desired concentration.

3) The solution is stirred for 3 hours at 70°C during which hydrolysis and condensation occur.

4) The solution is aged for 24 hours at room temperature.

5) The aged solution is then spin-coated on the silicon wafer to form a uniform layer.

6) The film is heat treated at 1000°C for 3 hours to form an erbium-doped silica glass.

The process is repeated multiple times until the desired silica-film thickness is obtained. Note that without step 2), the resultant film would be a pure sol-gel silica film.

A2. Fabrication of edge microtoroids. To investigate the PT-symmetric coupled-resonator system, we must be able to tune the coupling strength and/or the gain-to-loss ratio. The optical gain in the active resonator, which enables us to tune the gain-to-loss ratio, is provided by optically pumping the erbium ions with a pump laser[4,5]. The coupling strength is tuned by varying the distance between the two resonators[6]. This can be achieved by fabricating each of the resonators at the edge of a different chip and by controlling the
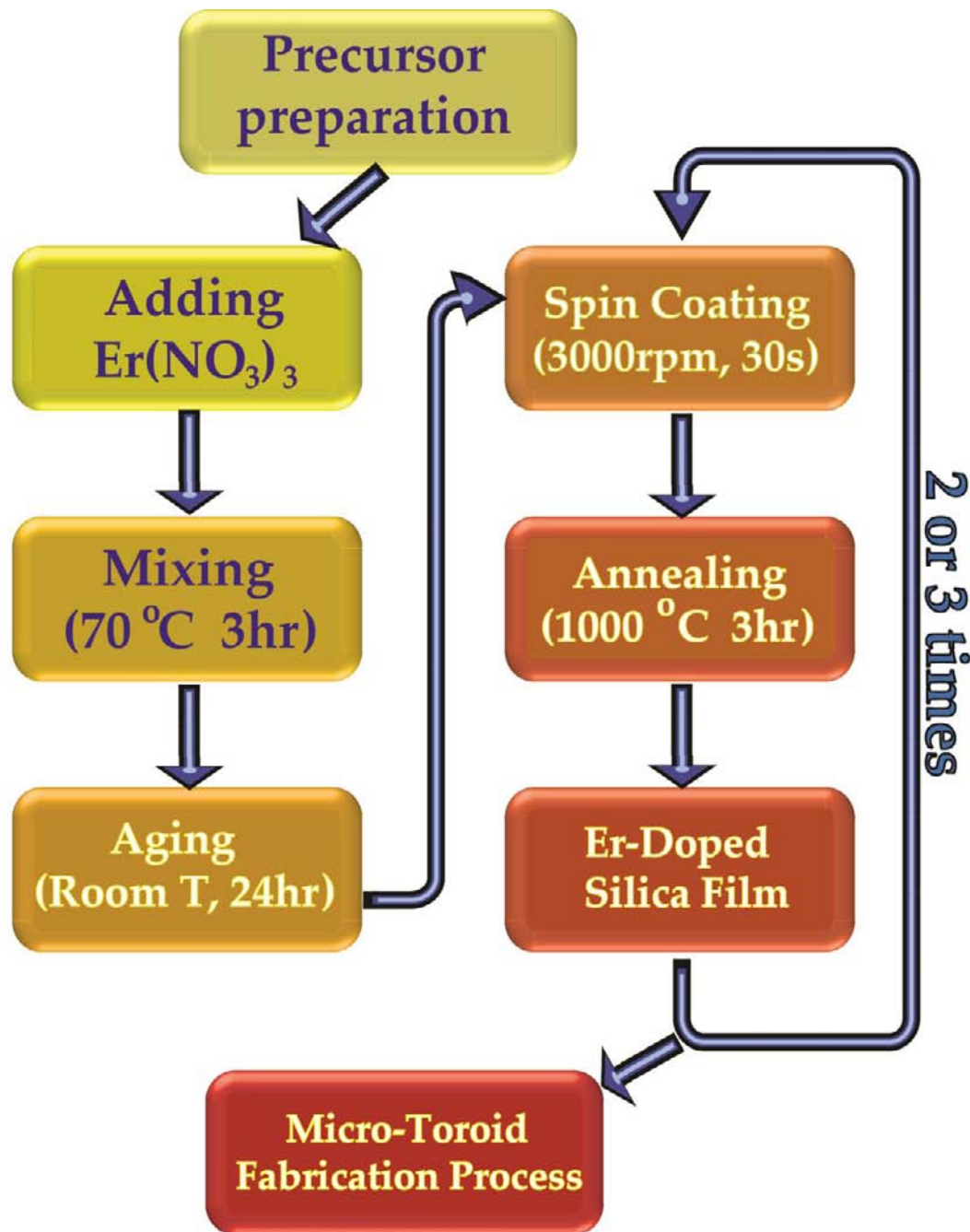
FIG. S1. **Preparation of erbium-doped silica film for fabrication of active WGM resonators.** *Any rare-earth ion, such as ytterbium, neodymium, and thulium, can be incorporated into the silica matrix using this process by replacing the $Er(NO_3)_3$ with a soluble compound containing the relevant ion. Without the additional step for rare-earth-ion or other gain material, the resultant film would be a plain sol-gel silica film.*
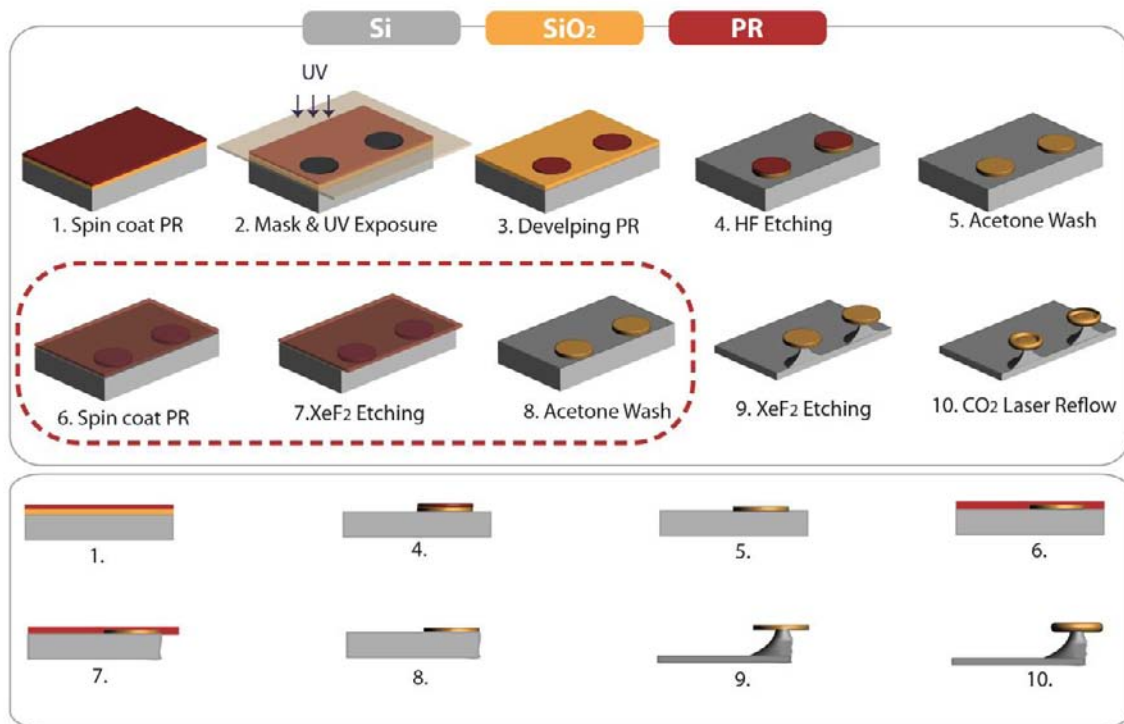
FIG. S2. Fabrication process of edge-microtoroids on silicon wafer. *Top (upper panel) and the side (lower panel) views of the resultant structure during the fabrication are shown. The fabrication steps 1-5, 9 and 10 are the steps for standard silica microtoroid fabrication on silicon wafer. The steps in the dotted box are necessary for obtaining the edge microtoroids, which stand on silicon pillars and hang over the silicon wafer. A passive silica edge-microtoroid is fabricated starting in step 1 with a thermal silica or sol-gel silica film on silicon wafer. Starting in step 1 with rare-earth-ion doped sol-gel silica film on silicon wafer, an edge active-microtoroid is fabricated. Si: silicon; SiO_2: silica; PR: photoresist; HF: hydrofluoric acid; XeF_2: xenon difluoride; CO_2: carbon dioxide (see text for details).*

separation between chips by using nanopositioning systems on which the chips are placed.

To fabricate the microtoroids at the edges of the chips, we modify slightly the original recipe for fabricating on-chip microtoroid resonators[1,7]. The process, which is illustrated in **Fig.S2**, is the same for both passive and active resonators. It begins with silica free of gain dopants on a silicon wafer for the passive resonator and with erbium-doped silica film on a silicon wafer for the active one. We fabricate the edge-toroids as follows:

1) A photoresist (PR) layer is spin-coated over plain silica (for the passive resonator) or erbium-doped sol-gel silica (for the active resonator).

2) Using UV-photolithography circular disks are patterned on the silica film.

3) PR is then developed, forming PR disks.

4) With hydrofluoric (HF) acid as the etchant, silica that is not covered with the PR is removed in order to form PR-coated silica disks on silicon wafer.

5) PR is then removed by washing the wafer with acetone, uncovering the silica disks.

6) and 7) A new layer of PR is spun coated on the wafer and then the chip is exposed to XeF_2 gas, which isotropically etches silicon. The PR layer forms a protective layer, so XeF_2 does not etch the structure from the top. Etching only proceeds in a direction parallel to the surface.

8) The PR is washed away with acetone. Steps 6)-8) are repeated until the desired over-hang disk structure is formed.

9) The wafer is immersed in XeF_2 gas once more to etch silicon from the top and sides in order to form the pillar structure, i.e., silica disks over silicon pillars.

10) Finally, CO_2 reflow heats and melts the silica disks, transforming them into silica microtoroids. The resulting structures are microtoroids at the edge of a silicon wafer with their pillars on the silicon substrate but with a portion of the silica torus extending beyond the wafer.

A3. Fabrication of fiber tapers for add-drop filter (ADF) configuration. A pair of tapered optical fibers is used to couple light into and out of the WGM resonators. The coupled resonator system is placed between two fiber tapers, similar to the standard add-drop-filter (ADF) configuration (**Fig. S3** and **Fig. S4B**). The fiber tapers should be parallel to each other and have similar waist size and mode profiles to achieve the best coupling. Their separation must be large enough to place the coupled resonators between them. To achieve these, the fiber tapers were fabricated by heating and stretching a pair of single mode silica fibers simultaneously over a hydrogen flame. The result was two fiber tapers with a very small height difference and ~90% transmission. We used a fiber-tip controlled with a

nanopositioner to push one of the fiber tapers away from the other until their separation was roughly equal to the sum of the diameters of the two resonators. The separation was adjusted by pushing the tapers towards or away from each other as well as to and from the resonators until the desired coupling conditions were achieved[8]. An additional nanopositioning stage was used to adjust the distance between the resonators.

B. Experimental setup and characterization of the PT-symmetric microcavities

B1. Experimental setup. Our experimental setup consists of seven ingredients (**Fig. S3**).

1) The coupled system of a passive and an active microtoroid. The resonators are directly coupled to each other in the 1550 nm band via their evanescent fields. There is no direct coupling between the resonators in the 1460 nm band.

2) A pair of tapered optical fibers to couple light into and out of the WGM modes of the resonator. Each tapered fiber is coupled to one resonator.
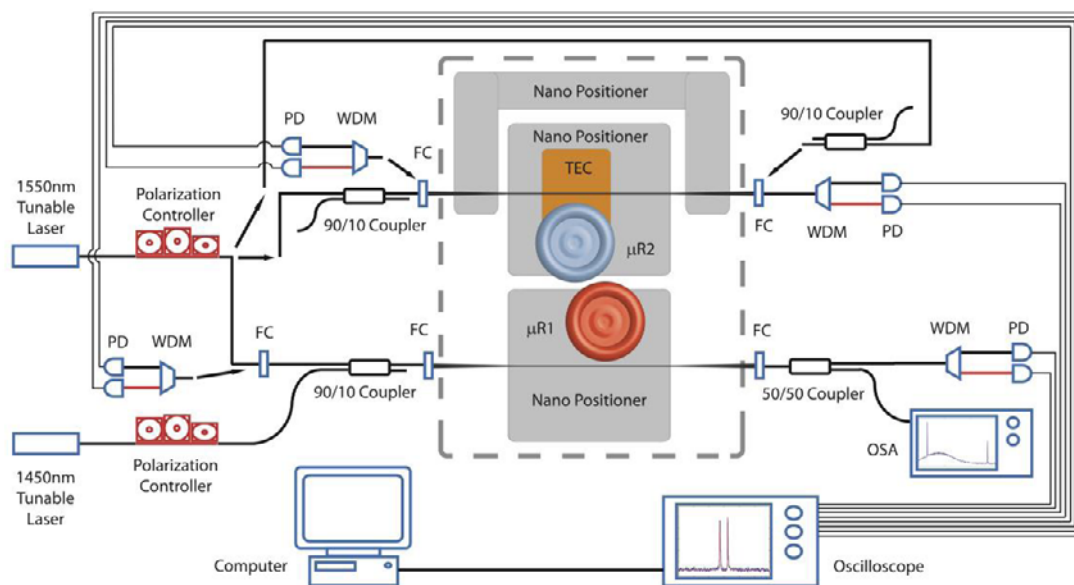

FIG. S3. Experimental setup used for the study of PT-symmetric whispering gallery mode (WGM) microcavities. μR1: active microtoroid; μR2: passive microtoroid; PD: photodetector; WDM: wavelength division multiplexer; FC: fiber connector; TEC: thermo-electric cooler; OSA: optical spectrum analyzer.
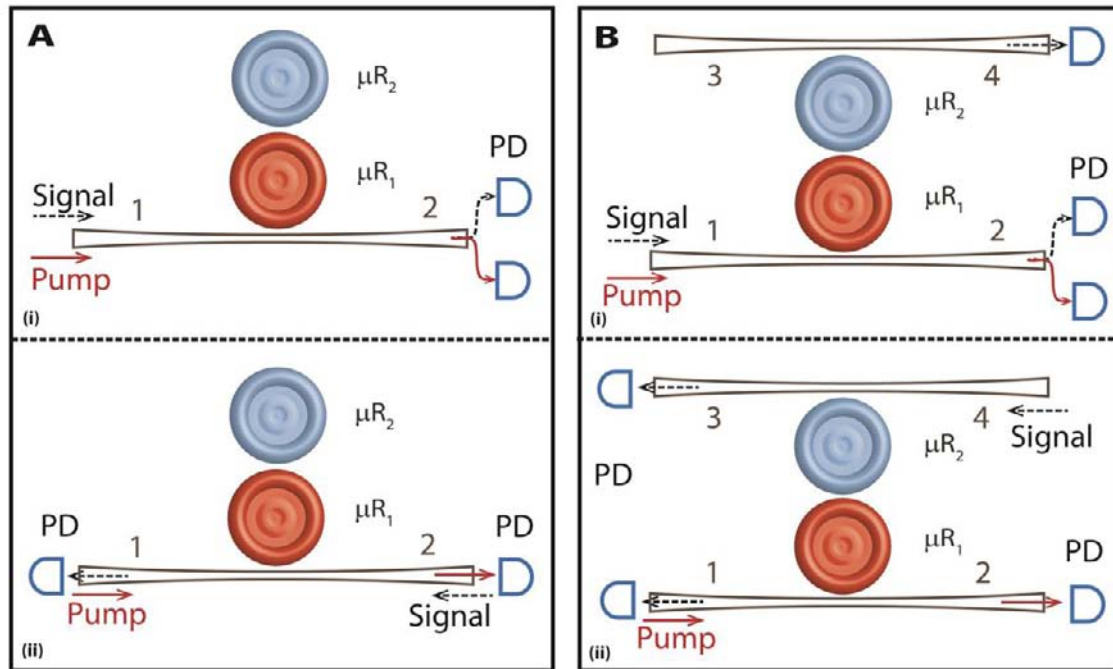
FIG. S4. *Illustrations of the setups used in the experiments.* (A) *Setup used to show the PT phase transition presented in Fig. 2 in the main text. [A(i) and A(ii)] correspond to two cases where the pump is input in the same (or opposite) direction as the probe signal, respectively. The results remain the same regardless of the pump direction. (B) Setup used for the demonstration of nonreciprocal light transmission as shown in Figs. 3 and 4 of the main text. [B(i) and B(ii)] respectively correspond to forward and backward transmission. μR₁: active microtoroid; μR₂: passive microtoroid; PD: photodetector. Signal probe and pump fields are denoted with different colors.*

3) Two external-cavity tunable laser sources. The first is used as the probe (signal) in the 1550 nm band; the second is in the 1460 nm band and is used to pump the erbium ions in the active microtoroid.

4) Nanopositioning systems to tune and adjust the coupling strengths between the resonators and fiber tapers as well as between the directly-coupled active and passive resonators.

5) Thermoelectric cooler (TEC) used to tune the resonance of the passive resonator via the thermo-optic effect. Initially, the resonances of the two resonators in the 1550 nm

band are spectrally separated from each other. Using the TEC, we tune one of the resonance lines of the passive resonator to overlap with a resonance line of the active resonator in the same band [6]. The resonators do not have overlapping resonance lines in the 1460 nm band, so the light from the pump laser is coupled only to the active resonator.

6) Photodetectors (PD) connected to an oscilloscope to monitor the transmission spectra at the outputs. Pump and probe light are separated using wavelength division multiplexers. An optical spectrum analyzer is used to characterize the optical gain and lasing from erbium ions.

7) A computer to process the transmission spectra and extract information on mode splitting (difference between the real parts of the eigenfrequencies of the coupled system) and the linewidth difference (difference between the imaginary parts of the eigenfrequencies of the coupled system) of the resonance lines.

We performed two sets of experiments using the setup in Fig. S3 in different subconfigurations by proper connections of the input and output ports:

a) By moving one of the fiber tapers far from the coupled system, we determined the unbroken- and broken-symmetry regions as a function of the coupling strength between the resonators and as a function of the gain-to-loss ratio (determined by the pump power). The results are shown in Fig. 2 of the main text. **Figure S4A** illustrates the scheme used here. Experiments were performed when the pump and probe (signal) are input in the same direction [Fig. S4A(i)] and when they are in opposite directions [Fig. S4A(ii)].

b) By using the ADF configuration, which is essentially a 2-by-2 optical device, we studied unidirectional light transmission (nonreciprocal optical transport). Figure S4B depicts the illustration of the scheme used here. The pump laser was input at port 1 and the probe (signal) was input at port 1 or at port 4. Transmission of the signal from port 1 to port 4 is the forward transmission whereas transmission from port 4 to port 1 is the backward transmission.

B2. Determining the coupling strength κ between the resonators. The coupling strength between the resonators is a function of the distance between them. In our experiments, we tune the distance between the resonators finely using a nanopositioning system with a step

resolution of 100 nm. In the following, we will introduce the theoretical framework for the determination and calibration of the coupling strength from the distance between the resonators. We performed the experiment using the configuration given in Fig. S4A(i) in which one of the resonators is directly coupled to an optical fiber waveguide. Defining the intracavity mode fields of the resonators as $a_{k=1,2}$ for the first and second resonators with resonance frequencies $\omega_{k=1,2}$, the coupling strength between the resonators as κ, and the input field as a_{in}, we can write the following rate equations for the coupled-resonators system

$$\frac{da_1}{dt} = -i\omega_1 a_1 - \frac{\gamma_1 + \gamma_c}{2} a_1 - i\kappa a_2 - \sqrt{\gamma_c} a_{in}$$
$$\frac{da_2}{dt} = -i\omega_2 a_2 - \frac{\gamma_2}{2} a_2 - i\kappa a_1 \tag{S.1}$$

together with the input-output relations $a_{out} = a_{in} + \sqrt{\gamma_c} a_1$. Here γ_k denotes the loss or gain of the resonators (loss: $\gamma_k > 0$; gain: $\gamma_k < 0$), and $\gamma_c > 0$ corresponds to the coupling loss between the first resonator and the fiber taper waveguide. The rate equations take the form

$$\frac{dA_1}{dt} = (i\Delta_1 - \frac{\gamma_1 + \gamma_c}{2})A_1 - i\kappa A_2 - \sqrt{\gamma_c} A_{in},$$
$$\frac{dA_2}{dt} = (i\Delta_2 - \frac{\gamma_2}{2})A_2 - i\kappa A_1 \tag{S.2}$$

after substituting $a_k = A_k e^{-i\omega t}, (k = 1,2)$ and $\frac{da_k}{dt} = -i\omega A_k e^{-i\omega t} + \frac{dA_k}{dt} e^{-i\omega t}$. Similarly, for the input-output relation we have $A_{out} = A_{in} + \sqrt{\gamma_c} A_1$. Here, $\Delta_{k=1,2} = \omega - \omega_k$ is the detuning between the resonance frequencies and the frequency of the input laser light. The coupling of these two resonators creates two supermodes $A_+ = (A_1 + A_2)/\sqrt{2}$ and $A_- = (A_1 - A_2)/\sqrt{2}$ with the eigenfrequencies ω_+ and ω_- given as

$$\omega_\pm = \frac{1}{2}i\left[-i(\omega_1 + \omega_2) - \frac{\gamma_1 + \gamma_c + \gamma_2}{2}\right] \pm \frac{1}{2}\sqrt{4\kappa^2 - \left[-i(\omega_1 - \omega_2) - \frac{\gamma_1 + \gamma_c - \gamma_2}{2}\right]^2} \tag{S.3}$$

Since in the experiments we tune the resonances of the resonators to be degenerate $\omega_1 = \omega_2 = \omega_0$, the eigenfrequencies can be re-written as

$$\omega_\pm = \left[\omega_0 - \frac{i}{4}(\gamma_1 + \gamma_c + \gamma_2)\right] \pm \frac{1}{4}\sqrt{16\kappa^2 - (\gamma_1 + \gamma_c - \gamma_2)^2} \tag{S.4}$$

where the expression in the square-root quantifies the effect of the coupling and the interplay between the coupling strength and the loss/gain in the resonators. Here we define the difference between the eigenfrequencies as the spectral distance

$$\delta = \omega_+ - \omega_- = \frac{1}{2}\sqrt{16\kappa^2 - (\gamma_1 + \gamma_c - \gamma_2)^2} \qquad (S.5)$$

There are four different regimes which are characterized by the interplay between the coupling strength and the total loss of the system. (i) No coupling between the resonators $\kappa = 0$. The resonance frequencies of individual resonators are equal and have the value ω_0, but their losses are different and quantified as $\gamma_1 + \gamma_c$ and γ_2 for the first and second resonators, respectively. (ii) Strong coupling regime where $16\kappa^2 > (\gamma_1 + \gamma_c - \gamma_2)^2$ is satisfied. In this case, the coupling between the resonators creates two supermodes, whose frequencies are up- and down-shifted by $\delta/2$ with respect to the initial resonance frequency ω_0 of uncoupled individual resonators, implying that supermodes are identified by the difference of their resonance frequencies. The transmission spectrum should exhibit two resonances (mode splitting) whose frequency difference (amount of splitting) increases with increasing coupling strength κ. Coupling does not induce extra loss and the linewidths of the supermodes are quantified by the sum of the losses of individual resonators. (iii) Critical coupling regime where $16\kappa^2 = (\gamma_1 + \gamma_c - \gamma_2)^2$. In this regime $\delta = 0$ and the resonance frequencies of the supermodes coalesce. (iv) Weak coupling regime where $16\kappa^2 < (\gamma_1 + \gamma_c - \gamma_2)^2$ is satisfied. Here, coupling induces extra loss to the system, and the two supermodes are identified by the difference in their linewidths.

We measure $\gamma_k > 0$ and $\gamma_c > 0$ in the experiments from the resonances in the transmission spectra (see Fig. 1d of the main text) of each resonator separately (i.e, without coupling between them). Note that γ_k is related with all the losses (scattering loss, bending loss and material loss) in the resonators except for the coupling losses. Thus we need to minimize the effect of the coupling losses on our transmission spectra measurements to derive γ_k. This is possible when the fiber-resonator coupling is set to deep-undercoupling regime where coupling loss is much smaller than the other losses in the system. In the deep-undercoupling regime, we obtain the transmission spectra for each of the resonators separately and then find

the linewidths $\Delta\omega_k$ and the resonance frequency ω_k of the mode of interest by Lorentzian curve fitting to the resonances obtained in the transmission spectra. Then we calculate the quality factor $Q_{k=1,2} = \omega_k / \Delta\omega_k = \omega_k / \gamma_k$ from which the loss parameter γ_k is calculated. In the configuration shown in Fig. S4A(i) and in the model expressed in Eq. S.1, the first resonator is coupled to a fiber taper; therefore, the resonator-fiber coupling loss should also be estimated in the experimental settings. In order to do this, we move the fiber taper from the deep-undercoupling regime closer to the critical coupling condition. This naturally induces loss and leads to the broadening of the linewidth of the resonance mode observed in the transmission spectrum of the first resonator. Under this condition, the measured quality factor is generally referred to as the loaded quality factor and expressed as $Q_{loaded}^{-1} = Q_1^{-1} + Q_c^{-1}$ where Q_c is the fiber-resonator coupling quality factor and denotes the coupling loss. In other words, loss parameters of the system satisfy $\gamma_{loaded} = \gamma_1 + \gamma_c$. Plugging in this expression the value of Q_1 (or γ_1) estimated in the deep-undercoupling regime for the first resonator and the newly estimated Q_{loaded} (or γ_{loaded}), we find Q_c (or γ_c) used in our experiments. Thus in the
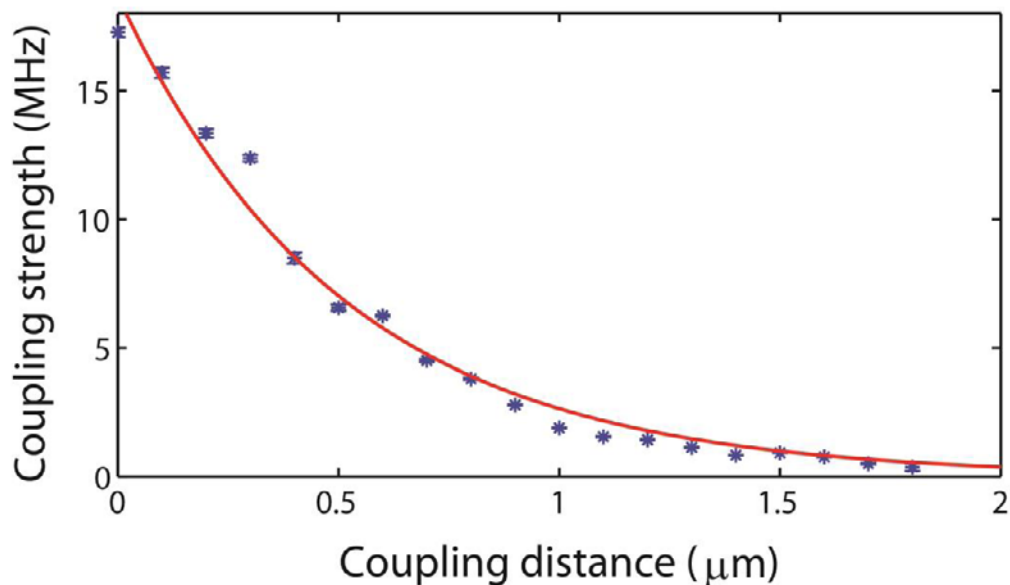

FIG. S5. Relation between the coupling strength κ and the distance between the microtoroid resonators. *The zero distance here corresponds to the case when the resonators are close to each other within the 100nm step-resolution of the nanopositioning system.*

expressions in Eqs. S.1-S.4, the only unknown parameter is the coupling strength κ between the resonators. Note that in the case of optical pumping of the active resonator, photons emitted from the gain medium provide gain to the resonance mode of the first resonator, leading an increase in Q_1 and decrease in γ_1 as seen in Fig.1e of the main text.

In the experiments, we monitored the change in the mode splitting (difference between the resonance frequencies of the supermodes) as the distance between the resonators is varied. From the experimentally obtained splitting, we estimated the value of κ using Eq. S.4. The resultant relation between κ and the distance between the resonators is given in **Fig.S5** where we see that the coupling strength exponentially decreases with increasing distance between the resonators. This result agrees well with previous reports in the literature[6,9,10]. A curve fitting method to estimate the coupling strength κ will be explained in the next section.

B3. Estimating eigenfrequencies of the supermodes from the experimentally obtained transmission spectra. Using the configuration given in Fig. S4A(i), we probed the transmission spectra of PT-symmetric coupled resonators system at different coupling conditions, and estimated the eigenfrequencies of the supermodes from the measured transmission spectra. This is done by curve fitting an analytical expression obtained for transmission using coupled-mode theory to the experimentally obtained transmission spectra. Starting with the expressions given in Eqs. S.1-S.2 and the input-output relation for the system, we find the steady-state normalized transmission $T = \left| A_{out} / A_{in} \right|^2$ as

$$T = \left| 1 - \frac{2\gamma_c \left(\gamma_2 - i2\Delta \right)}{4\kappa^2 + \left(\gamma_1 + \gamma_c - i2\Delta \right)\left(\gamma_2 - i2\Delta \right)} \right|^2 \tag{S.5}$$

where γ_1, γ_2 and γ_c are all known from the experiments as explained above, and we used $\omega_1 = \omega_2 = \omega_0$ and $\Delta = \omega - \omega_0$ because in the experiments the resonance frequencies of the resonators are set to be equal using thermal tuning via the thermo-optic effect. We used the expression in Eq. S.5 as the curve fitting function to the experimentally-obtained transmission spectra under different coupling strengths κ (i.e., distance between the resonators). Note that for the ideal PT-symmetry case in which gain in the active resonator equals to loss in the passive one (i.e., $\gamma_1 + \gamma_c < 0$, $\gamma_2 > 0$ and $\gamma_1 + \gamma_c = -\gamma_2$), Eq. S.5 becomes

$$T_{\gamma_1+\gamma_c=-\gamma_2} = \left| 1 - \frac{2\gamma_c\left(\gamma_2 - i2\Delta\right)}{4\kappa^2 - \left(\gamma_2^2 + 4\Delta^2\right)} \right|^2 \tag{S.6}$$

When there is no gain in the system (coupled passive resonators), all the parameters except for κ are known. Therefore, curve fitting the expression in Eq. S.5 to the experimentally-obtained transmission spectrum with κ as the free parameter provides a value for κ which is then used in Eq. S.4 to obtain the eigenfrequencies of the two supermodes. When the gain is present in the system, we used κ and γ_1 as the free parameters for curve fitting. The estimated values of κ and γ_1 are used in Eq. S.4 to obtain the supermode eigenfrequencies.

In **Fig. S6**, we provide the experimentally obtained transmission spectra together with the fitted curves using Eq. S.5 and the eigenfrequencies estimated via Eq. S.4. Clearly, even if the resonances coalesce as shown in Fig. S6A, the theoretical fit provides two different eigenfrequencies distinguished by the difference in their linewidths. The confidence of the curve fitting was always larger than 0.95.
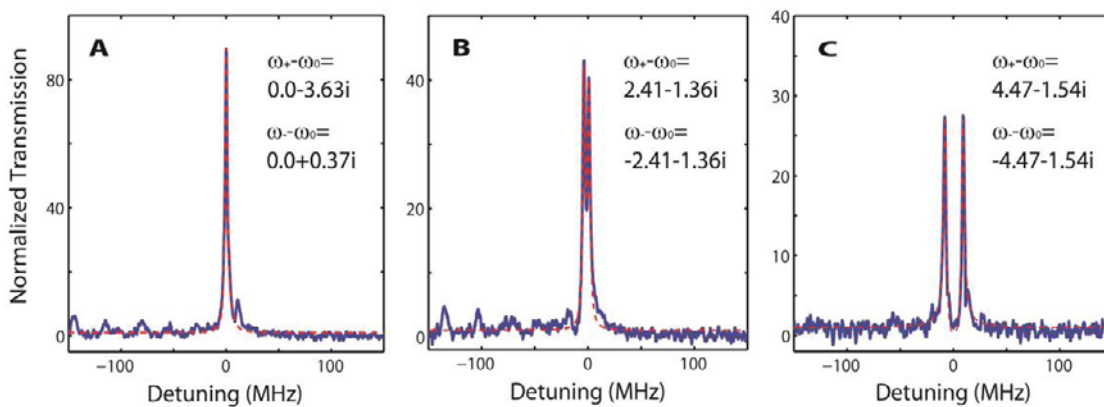

FIG. S6. Theoretical curve fitting to extract the eigenfrequencies in the broken-PT-symmetric phase. *We fitted the transmission function obtained from the theoretical model and given in Eq. S.5 to the transmission spectra obtained in the experiments. Estimated coupling strengths* κ *and gain-loss parameter* γ_1 *are (**A**)* $\kappa = 2.95\ MHz$ *and* $\gamma_1 = -13.84\ MHz$ *, (**B**)* $\kappa = 4.16\ MHz$ *and* $\gamma_1 = -13.07\ MHz$ *, and (**C**)* $\kappa = 9.75\ MHz$ *and* $\gamma_1 = -14.55\ MHz$ *. The detunings of the calculated eigenfrequencies from the initial resonance frequencies are given in the inset and the units are in MHz. Blue denotes the experimental data and red denotes the best fit.*

B4. Threshold coupling strength κ_{PT} . In Fig. 2 of the main text and Fig. S7 of this Supplement, we plotted the real and imaginary parts of the eigenfrequencies as a function of the parameter κ / κ_{PT} where κ is the coupling strength as discussed above. Here κ_{PT} is the threshold coupling strength at which the real parts of the eigenfrequencies of the supermodes coalesce for the first time and become equal for a fixed gain and loss ratio as the coupling strength κ (i.e., distance between the resonators) is decreased. Then the value of κ satisfying $16\kappa^2 = \left(\gamma_1 + \gamma_c - \gamma_2 \right)^2$ is the threshold coupling strength κ_{PT} , which is found as

$$\kappa_{PT} = \frac{1}{4}\left| \gamma_1 + \gamma_c - \gamma_2 \right| \qquad (S.7)$$

It is clear that κ_{PT} depends on the gain-loss ratio of the coupled system. For the ideal case when gain and loss are balanced (i.e., $\gamma_1 + \gamma_c = -\gamma_2$), the threshold coupling constant κ_{PT} becomes

$$\kappa_{PT} = \frac{1}{2}\gamma_2 \qquad (S.8)$$

If one can measure γ_1 , γ_c and γ_2 precisely then the κ_{PT} can be calculated using Eq. S.7. However, in an experiment, especially when there is gain in the system, one does not know the exact value of γ_1 and may not achieve exactly balanced loss and gain. Moreover, in scheme like ours, the coupling strength that can be probed is limited by the step resolution of 100 nm of the nanopositioning system. Therefore, satisfying the above expression exactly is difficult.

In the experiments, we first bring the loss and the gain as close to each other as possible, and then monitor the transmission spectra as we decrease the coupling strength κ by increasing the distance between the resonators. At each value of distance (i.e., our nanopositioning system has a step resolution of 100 nm), we obtain the transmission spectrum and then estimate the coupling strength κ and γ_1 via the curve fitting as described in section B3. Then using the estimated value of κ and γ_1 , we calculate the real and imaginary parts of the eigenfrequencies. The value of κ at which the real parts of the eigenfrequencies become the same for the first time as κ is decreased (i.e., distance between the resonators is increased) is the value of κ_{PT} . Due to the limited resolution of our nanopositioning system, in the experiments we may miss the exact point where $16\kappa^2 = \left(\gamma_1 + \gamma_c - \gamma_2 \right)^2$ is satisfied.

Therefore, we need to estimate κ_{PT} from the available information. In the experiments, we found out that the value of γ_1 is almost constant as it should be because we keep the gain condition constant by fixing the pump power of the gain medium. Slight fluctuations γ_1 come from fluctuations of the pump power and frequency. From these experiments, we assigned an average value to γ_1. Then we used this value in Eq.S.7 to calculate κ_{PT}. We checked the validity of the calculated κ_{PT} by confirming that it falls between two experimentally accessible κ values κ_1 and κ_2 which satisfy $16\kappa_1^2 > (\gamma_1 + \gamma_c - \gamma_2)^2$ and $16\kappa_2^2 < (\gamma_1 + \gamma_c - \gamma_2)^2$, (i.e., $\kappa_1 > \kappa_{PT} > \kappa_2$).

In Figs. 2c and 2d, we compare the evolution of the real and imaginary parts of the eigenfrequencies of the supermodes for two different values of the loss in the second resonator. The value of κ_{PT} used in these figures was obtained for the case of high quality factor $Q=3.0\times10^7$ resonance mode (resonance mode with lower loss) of the second resonator μR_2 in order to visually compare the symmetry breaking points of these two different cases. Therefore, the symmetry breaking point for the case of lower loss appears at $\kappa/\kappa_{PT}=1$ whereas that for the case with higher loss appears at $\kappa/\kappa_{PT}>1$. This confirms that the higher the loss in the passive resonator the higher the threshold for symmetry breaking point, as quantified in Eqs. S.7 and S.8.

B5. Typical transmission spectra in the broken- and unbroken-symmetry regions. Using the configuration given in Fig. S4A(i), we probed the transmission spectra of the coupled-resonators system as a function of the coupling strength after setting the gain and loss as close to each other as possible. The results showing the PT-symmetry breaking are provided in Fig. 2 of the main text. In **Fig. S7**, we provide typical transmission spectra obtained in our experiments for the broken- and unbroken-symmetry phases shown in Fig.2 of the main text.

B6. Co- and counter-propagating pump and probe light. In order to check the effect of the direction of the pump on the observed PT-symmetric phenomena, we performed experiments using the configuration in Fig.S4A(i) and (ii). Typical experimentally-obtained transmission spectra in the broken- and unbroken-PT symmetry phases are given in **Fig. S8**. It is clear that

regardless of the propagation direction of the pump laser with respect to the probe, the same behavior is observed. This can be explained as follows. WGM resonators support counter-propagating frequency-degenerate modes, so light emitted from excited erbium ions during their transition to the ground state can couple to modes propagating in clockwise and counter-clockwise directions with equal probability. Thus, regardless of the propagation direction of the pump, the weak probe signal is always amplified.
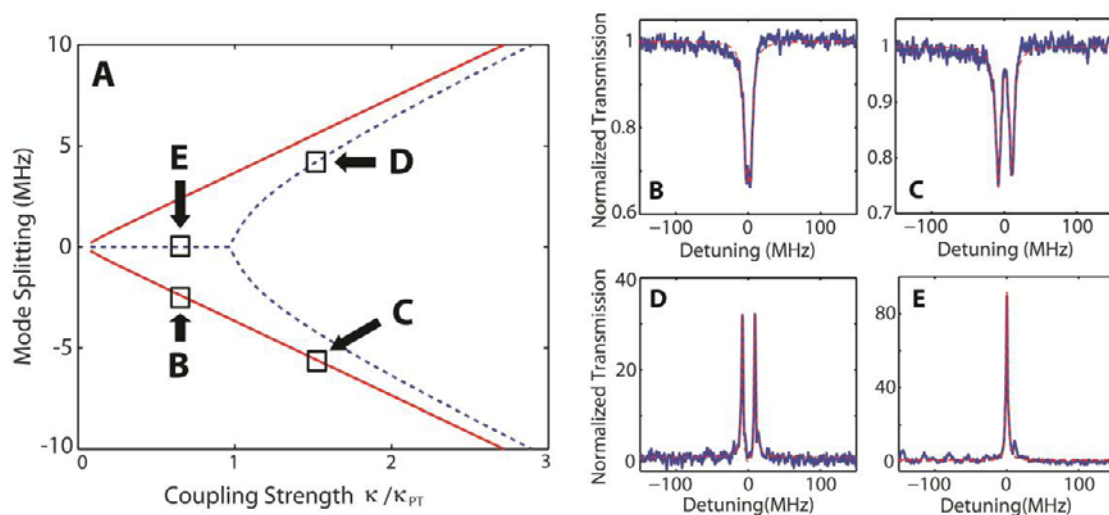

Fig. S7. Experimentally obtained transmission spectra in broken-PT- and unbroken-PT-symmetric regions. *The configuration shown in Fig. S4A(i) is used. (A) Mode-splitting, corresponding to the difference between the real parts of the eigenfrequencies of the supermodes of the coupled WGM-resonator system, as a function of the coupling strength. The coupling conditions labeled with square marks and letters (B)-(E) are the conditions for which transmission spectra are given in panels (B)-(E). The straight red lines in (A) depict the case in which both resonators are passive; the dotted blue lines depict the case in which one resonator is active and the other is passive with balanced loss and gain. (B) Both resonators are passive (no gain) and the coupling is small. Splitting is barely seen. (C) Both resonators are passive and the coupling is strong. Mode-splitting is clearly seen. (D) Coupled passive and active resonators in the unbroken-symmetry region. Split resonance peaks are clearly seen. (E) Coupled passive and active resonators in the broken-symmetry region, showing the coalescence of the supermodes.*
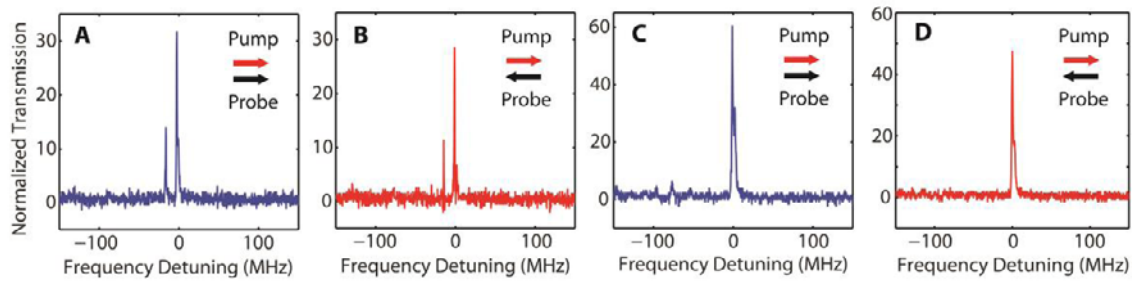
Fig.S8. Experimentally obtained transmission spectra in broken- and unbroken-PT-symmetric regions with different pump and probe directions. In these experiments the configurations in Fig. S4A are used. (A) and (B)are obtained in the unbroken-symmetry region using Fig. S4A(i) and Fig. S4A(ii), respectively. (C) and (D)are obtained in the broken-symmetry region using Fig. S4A(i) and Fig. S4A(ii), respectively. The transmission spectra are the same regardless of the directions of the pump and probe light fields.

B7. Localization of field in the active resonator in the broken PT-symmetry phase. Strong nonreciprocity observed in our PT-symmetric optical resonators is due to the significant enhancement of nonlinearity in the broken symmetry phase. This enhancement, on the other hand, originated from the strong field-localization in the broken symmetry phase. Field localization here means that regardless of which port is used as the input port, the field is always localized in the active resonator (i.e., resonator with gain and with less loss). Therefore, the signal at the output port of the fiber taper coupled to this active resonator shows a strong resonance peak whereas the signal at the output port of the fiber taper coupled to the passive resonator (i.e., resonator without gain) is minimized, if not completely eliminated. This is true regardless of whether the input is at the fiber taper waveguide coupled directly to the passive or the active resonator. The results of our experiments are depicted in **Fig. S9** where we see that only when the PT-symmetry is broken, the field is localized in the active resonator and thus the signal at the output port of the fiber coupled to it shows a strong resonance peak whereas there is a complete absence of resonance peaks at the output of the fiber coupled to the passive resonator. In the unbroken phase, both outputs show resonance peaks regardless of the input port.

When there is no gain in the system (both resonators are passive), the output of the fiber through which the field is input shows a resonance dip and the output of the other fiber shows

a resonance peak [**Fig. S9A(a)** and **S9B(a)**]. Resonance dip at port 2 (4) for the input at port 1 (3) is due to destructive interference between the light transmitted directly to the output and the portion coupled to the resonator and then coupled back to the fiber. A portion of the light coupled to the resonator from the input fiber then couples to the other resonator and leaks to the output port of the other fiber, leading to resonance peaks.
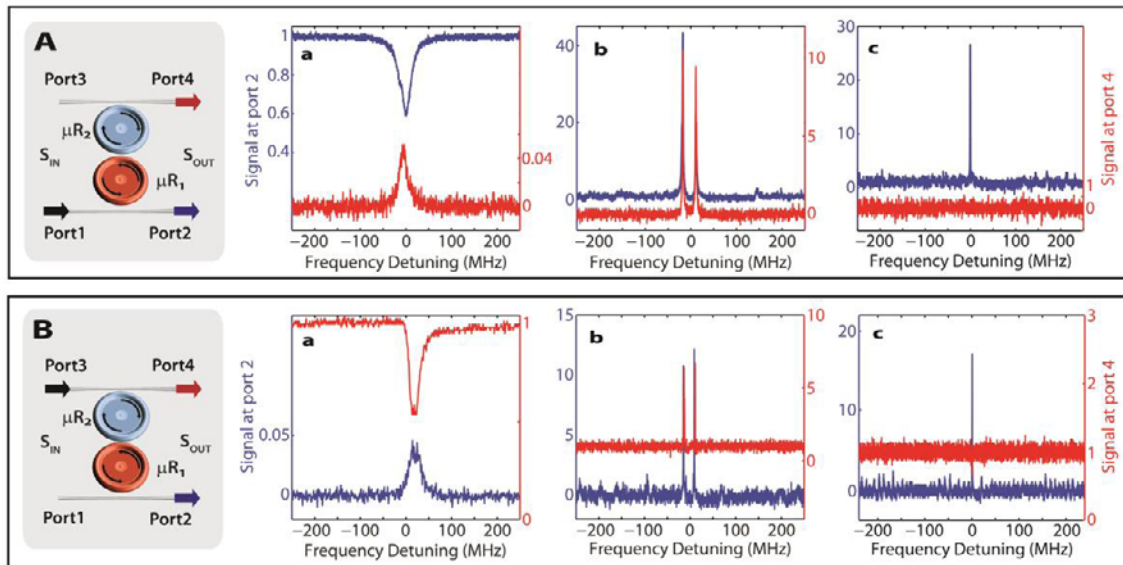

Fig.S9. Localization of the optical field in the active resonator in the broken-PT symmetry phase. *Fiber taper waveguide with ports 1 and 2 is coupled to the active resonator whereas the one with ports 3 and 4 is coupled to the passive resonators. (A) Input is at port 1 (active resonator side), and outputs are measured at ports 2 and 4. (B) Input is at port 3 (passive resonator side), and outputs are measured at ports 2 and 4. [A(a)] and [B(a)] denote the case when there is no gain in the system, [A(b)] and [B(b)] correspond to the case where the gain and loss of the system is balanced and the system is in unbroken-PT-symmetric phase because coupling strength is large, and finally [A(c)] and [B(c)] correspond to the case where the gain and loss of the system is balanced and the system is in the broken-PT-symmetric phase due to the weaker coupling strength between the resonators. Blue curves denote the output at port 2 and red curves denote the output at port 4. It is clear that in the broken PT-symmetric phase, the field is always localized in the resonator with gain or with low loss, regardless of whether the input is at the passive resonator side or at the active resonator side.*
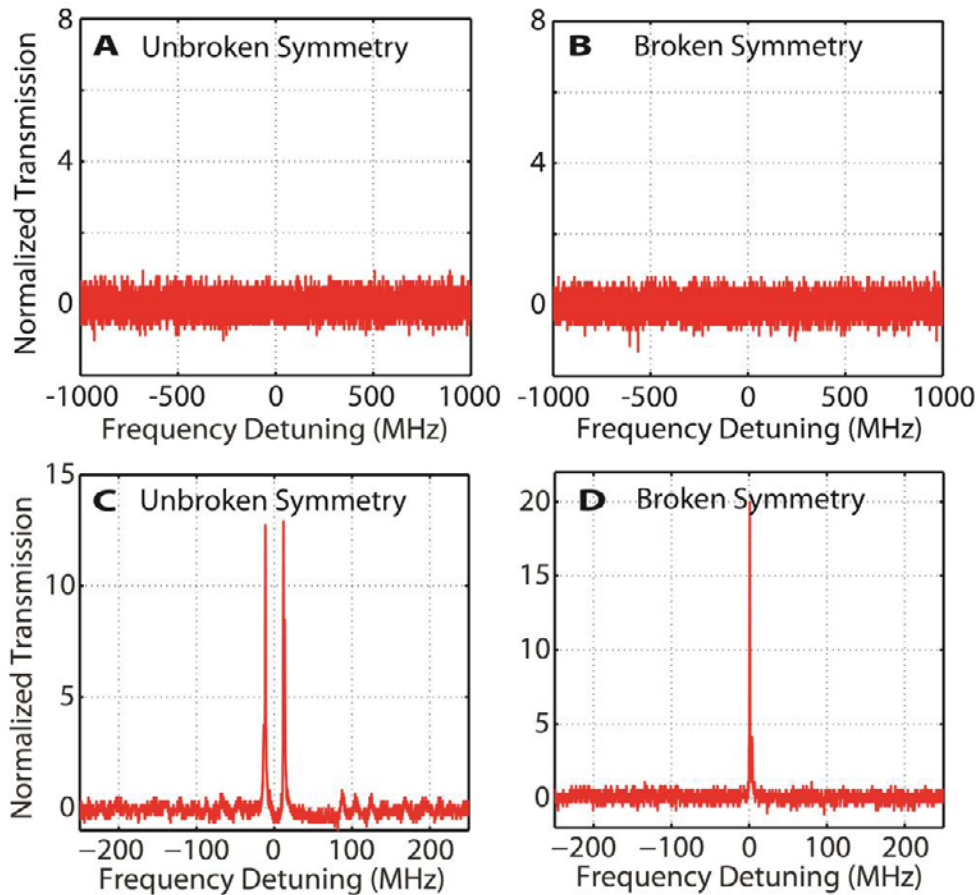
Fig. S10. Experimentally obtained spectra showing the effect of the weak signal at the input port on the output transmission spectra. *This is an enlarged version of the spectra shown in Figs. 4[b(ii) and b(iii)] for the backward transmission as depicted in Fig. S4B(ii). For both the unbroken- and broken- symmetry cases, the output port 1 remains at the noise level without any observable resonance peak when there is no weak signal at the input port 4 (**A** and **B**). When a weak signal is input at port 4, resonance enhancement is observed for both the unbroken- and broken-symmetry cases (**C** and **D**).*

When the gain and loss are balanced but the coupling strength is large (distance between the resonators is small) such that the system is in the unbroken PT-symmetric phase [**Fig. S9A(b)** and **S9B(b)**], the outputs always show two resonance peaks (mode splitting) regardless of whether the field is input at port 1 or port 3. The split resonance modes have the same resonance frequencies and similar linewidth in both of the cases, except with slight variations in their heights.

When the gain and loss are balanced and the coupling strength is weak (distance between the resonators is large) such that the system is in the broken PT-symmetric phase [**Fig. S9A(c) and S9B(c)**], only the output port 2 shows a resonance peak regardless of whether the input is at port 1 or at port 3. No resonance peak or dip is observed in the output port 4 in both cases. This implies that the input field is localized in the active resonator which is directly coupled to the fiber taper with the ports 1 and 2.

B8. Effect of the weak probe signal on the output spectra. In **Fig. S10**, we give enlarged spectra of those shown in Figs. 4[b(ii) and b(iii)] of the main text. It is clear that when there is no weak signal at the input port, the output port remains at the noise level with no observable resonance dip or peak because our system is driven below the lasing threshold. One can say that the photons emitted by the excited ions are consumed by the losses (intrinsic and coupling losses) in the system. With the weak signal at the input port, we see a resonance enhancement at the output port for both the broken- and the unbroken-symmetry cases.

B9. Supplementary experimental data for nonreciprocal light transmission. For the demonstration of nonreciprocal light transmission in our PT-symmetric system, we used the configuration given in Fig. 4S(B). We defined the transmission from port 1 to port 4 as the forward $T_{1\rightarrow4}$ and transmission from port 4 to port 1 as the backward $T_{4\rightarrow1}$ transmission. In the main text, we provided the results for the $T_{1\rightarrow4}$ and $T_{4\rightarrow1}$ demonstrating that in the broken-symmetry region, forward transmission reduces to zero $T_{1\rightarrow4} \sim 0$ [Fig. 4a(iii)] but the backward transmission remains high [Fig. 4b(iii)]. In the experiments, we monitored ports 2 and 4 when the input was at port 1, and ports 1 and 3 when the input signal was at port 4. In Fig. 4 of the main text, we provided only the spectra at port 4 (1) when the signal input was at port 1 (4). In **Fig. S11** below, we provide the transmission spectra at ports 2 (3) when the input signal is at port 1 (4) to give a clear understanding of the signal at the other ports. In the broken-symmetry region, for forward propagation we observe amplified signal at output 2 at resonance while the signal at output 4 is almost zero. For backward propagation, the amplified signal is at port 1; however, the signal at port 3 has a shallow resonance dip.

B10. Fluctuations in the heights of resonance peaks. In Fig. 3c (unbroken phase) of the main text and in Fig. S11, the heights of the doublets (peaks) for the backward and forward transmission show a difference. This difference is attributed to a number of different issues in our system. First, the frequency and the output power of our lasers are not actively controlled or stabilized. During the scanning of the laser frequency to obtain the transmission spectra, the outputs of the lasers fluctuate which is reflected as the fluctuations at the heights of the peaks or dips at the resonance frequency. Second, since we do not have active stabilization and control mechanisms, there are fluctuations such as thermal fluctuations which swing the resonances slightly changing the measured output signal. In **Fig. S12**, we provide a set of experimental results obtained on the same setup under the same conditions but at different
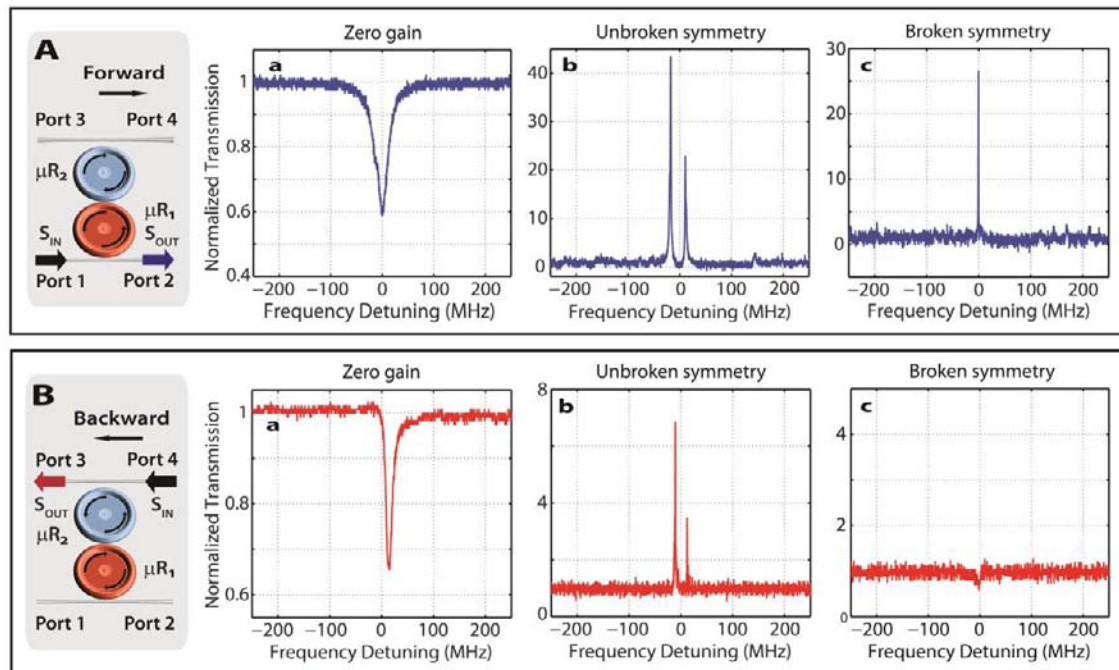

Fig.S11. Experimentally obtained spectra in broken- and unbroken-symmetry regions. *(A) Output at port 2 when the input signal is at port 1 for passive photonic molecule [A(a)], in PT-symmetric system when the symmetry is unbroken [A(b)]and when it is broken [A(c)]. Output at port 4 is given in Fig. 4a of the main text. (B) Output at port 3 when the input signal is at port 4 for passive photonic molecule [B(a)], in PT-symmetric system when the symmetry is unbroken [B(b)]and when it is broken [B(c)]. Output at port 1 is given in Fig. 4b of the main text.*

times. As it is seen, due to the above issues, the heights of the peaks fluctuate; they sometimes have the same heights but at some other times one is higher than the other.

The crucial thing to point out here is that even if there are fluctuations in the heights of the peaks for backward and forward transmissions in the broken and unbroken phases in the linear regime (Fig. 3c of the main text), there is no complete absence of transmission peak in one direction. The peaks always stay there regardless of the fluctuations. Note that when the system is driven to the nonlinear regime, for the broken phase, we see complete absence of transmission peak in the forward direction (Fig. 4a of the main text). Similarly, even if there are slight fluctuations in the spectra obtained at different times in the broken phase in the nonlinear regime for forward and backward transmission, there is always a strong transmission in one direction and complete absence of the peak in the other direction. Such fluctuation can be minimized, if not completely eliminated, by active stabilization and control of laser frequencies and output powers and thermal fluctuations in the environment, etc.
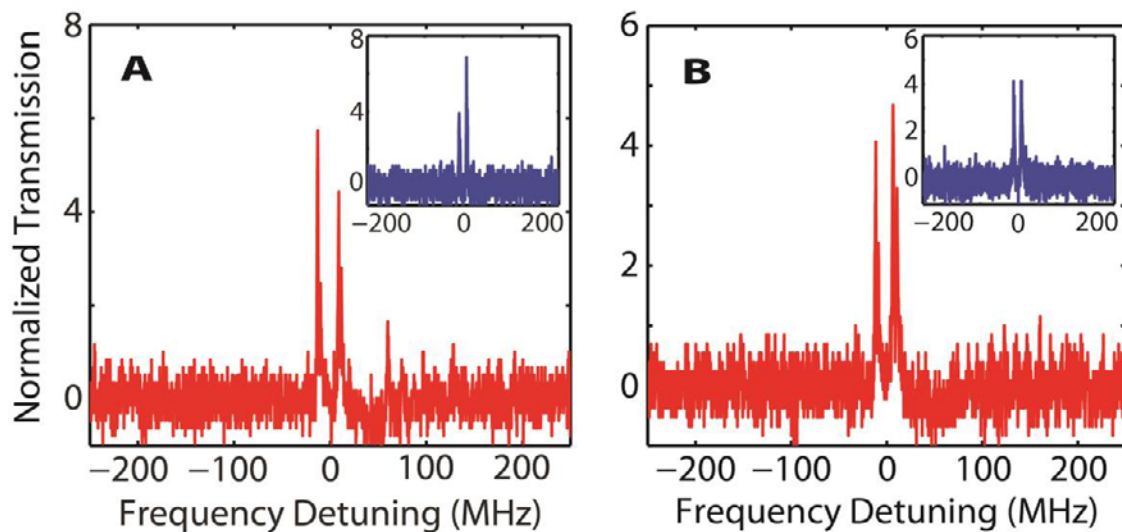

Fig.S12. Transmission spectra obtained at different times when the system is in the linear regime. *Although the heights of the resonance peaks fluctuate in measurements taken at different times, there are always two resonance peaks (split modes) in the backward transmission (red spectra) and forward transmission (blue spectra in the inset) directions when the system is in the linear regime and PT-symmetry is unbroken.*

B11. Comparison of nonreciprocity demonstrated in PT-symmetric microresonators with reported experiments utilizing nonlinearity or resonators. Many components or systems used in optics are reciprocal, i.e., light can be transmitted in both directions. Nonreciprocal devices are of great importance and much needed for optical communication and optical signal processing. For example, isolators are used to protect the laser sources and sensitive components from back-reflected light; circulators are used to separate and route light in bidirectional systems. The ability to control the direction of light flow in such a way that light is transmitted in one direction but blocked in the other direction requires breaking reciprocity or the time-reversal symmetry. In many optical systems used today, this is achieved using magneto-optical effects induced by applied magnetic fields. Unfortunately, magneto-optic effect in many materials is very weak. As a result, magneto-optic materials with large sizes and high magnetic fields are needed. These make the systems complicated and bulky. As the technology progresses drastically, there is a drive and tendency to make the systems smaller and smaller, and if possible to achieve on-chip optical processing systems with nano- or micro-scale footprints. The absence of magneto-optic effects in materials used in conventional optoelectronics processing demands that materials with higher magneto-optic effect are suitably integrated into the on-chip nano-or micro-scale structures. However, this is not an easy task. Therefore, there is an ever-increasing need for non-magneto-optic approaches to achieve nonreciprocal light transmission. Today it is well-known that reciprocity can be broken in magneto-optic materials, nonlinear materials and materials whose dielectric permittivity and magnetic permeability depend on time. In other words, a linear static dielectric system cannot have nonreciprocal response[11,12]. This is true even when gain and loss exist in the system[11]. Therefore, a system without magneto-optics has to rely on either nonlinearity or time-dependent effects to break time-reversal symmetry. In the following, we will introduce some of the beautiful experiments demonstrating nonreciprocal light transmission and compare their performance with the nonreciprocity achieved in our work, which brings PT-symmetric concepts with nonlinearity in coupled optical microresonators. Our focus is on demonstrations of nonreciprocity in on-chip waveguides and microresonators, and nonreciprocity based on nonlinear effects in different structures.

B11a. Nonreciprocity based on nonlinear effects. Despite many theoretical proposals, there exist only a very small number of experimental demonstrations of nonreciprocal light transmission based on nonlinear effects such as second-order nonlinearity $\chi^{(2)}$, Kerr-

nonlinearity $\chi^{(3)}$ and parametric nonlinearity. Raman amplification in silicon waveguides[13,14], stimulated Brillouin scattering in silica fiber[15] and dispersion-engineered chalcogenide waveguides[16], $\chi^{(2)}$ in asymmetric waveguides[17] and periodically poled lithium niobate waveguide[18], and a nonlinear, asymmetric, distributed Bragg reflector made from multilayer nonlinear thin film[19], stimulated inter-polarization scattering in a photonic crystal fiber[20], and thermal nonlinearity in a pair of silicon microring resonators[21], just to name a few. Among these there are three experimental demonstrations[18,20,21] that we will briefly summarize below.

Gallo *et al.*[18] demonstrated nonreciprocal behavior relying on the tailoring of second order nonlinearity $\chi^{(2)}$ with quasi phase matching gratings in a $LiNbO_3$ channel waveguide. The gratings were 4 cm long and had a period of 14.7 μm. Moreover, at each end of the channel waveguide 1-mm-long mode filters and 1.5-mm-long mode tapers were fabricated. In this device, nonreciprocity was observed for input peak powers beyond 1.5 W at λ=1.55μm. The contrast, defined as the difference between backward and forward transmissions normalized by the sum of the transmissions in both directions at the wavelength of interest, reached values as high as C=0.9 at an input power of P=3.1 W. Insertion loss of the device was ~0.7 dB/cm.

Kang *et al.*[20] showed nonreciprocal light transmission in a photonic crystal fiber (length of 1.5 m and a core of 1.8μm). Here breaking the reciprocity was achieved via the stimulated inter-polarization scattering (SIPS) which is a nonlinear process relying on optical excitation of a gigahertz guided acoustic mode. In SIPS, photons from a pump wave travelling in the forward direction scatter into the co-propagating but orthogonally polarized Stokes wave via the excited guided acoustic resonance. Thus in the forward direction the pump is strongly attenuated. However, if the pump is launched in the backward direction and counter-propagates with the Stokes wave, then SIPS does not take place and the pump is transmitted with a slight attenuation due to the fiber transmission loss. An extinction ratio of 20 dB was demonstrated for powers of ~ 0.31W.

Fan *et al.*[21], on the other hand, used a system of two silicon microring resonators with quality factors of Q~ 27,000 and Q~ 43,800 configured in an add-drop filter geometry and asymmetrically coupled to two optical waveguides to demonstrate nonreciprocal light transmission. In silicon resonators, two photon absorption (TPA), $\chi^{(3)}$ and thermal

nonlinearity are among the processes that can lead to the observed nonreciprocal behavior. The authors claimed that in their system thermal nonlinearity was the main reason for the observed behavior. As a result with input powers of P=85 μW and P=850 μW, nonreciprocal transmission ratios of ~20 dB and ~27 dB were demonstrated. The forward insertion loss of the device was 12 dB.

B11b. Nonreciprocity in optical microresonators. In addition to the experimental work by Fan *et al*. where nonreciprocity relies on thermal nonlineaity in silicon microring resonators and our present work which relies on nonlinearity enhancement in broken PT-symmetry phase for nonreciprocal light transmission, there are two more experimental works related with optical microresonators worth mentioning here: The works by Bi *et al*.[22] and Tien *et al*.[23] where magneto-optical materials are integrated with microresonators. We should mention that there are many proposals on how nonreciprocity can be achieved by integrating magneto-optical materials into microresonators, waveguides and photonic crystal structures either using sputter deposition[24], wafer bonding[25] or adhesive bonding[26]. The concept of nonreciprocal ring microresonator was introduced by Kono *et al*.[27] to reduce the size of isolators and other nonreciprocal devices down to several tens of micrometers and to achieve on-chip nonreciprocal devices. Here we will introduce only the works by Bi *et al*.[22] and Tien *et al*.[23] which rely on frequency splitting upon the application of magnetic field to silicon microresonators with the integrated cerium-substituted yttrium iron garnet (Ce:YIG) films. Whispering gallery mode resonators or the ring resonators support two counter-propagating modes (clockwise CW and counter-clockwise CCW) at the same frequency. An magnetic field applied to the magneto-optical microresonator breaks the symmetry of the resonator and lifts the frequency degeneracy[22,23,28]. As a result, the CW and CCW modes have different propagation constants and resonance frequencies, thus leading to non-reciprocal optical transmission in the wavelength range near the cavity resonance.

In their work[23] Bi *et al*. integrated a 100 nm garnet film layer Ce:YIG(80 nm)/YIG(20 nm) using a pulsed laser deposition technique onto a silicon racetrack resonator. They then lifted the degeneracy of CW and CCW resonant modes by applying a magnetic field perpendicular to the direction of light propagation. An extinction of 19.5 dB was achieved by a magnetic field strength of 1,500 Oe.

Tien *et al*.[23] integrated Ce-YIG of thickness 500 nm on the top of a silicon microring resonator of radius 900 μm using oxygen plasma enhanced bonding. They achieved an

extinction of 9 dB in the 1550 nm wavelength band with an applied magnetic field strength of 50 Oe.

B11c. Other interesting methods to achieve nonreciprocity. Among many other interesting approaches to achieve nonreciprocal light transmission, the works relying on opto-mechanical[29,30] effects and interband photonic transitions[31,32] are worth mentioning here.

In their work Manipatruni *et al.*[29] showed that optomechanical systems can exhibit nonreciprocity via momentum exchange during the interaction of the light field with the mechanical structure. The nonreciprocity originates from the asymmetry of the radiation pressure induced by the photons in the light field on a movable mirror for incident light in opposite directions. They then propose a silicon based micro-optomechanical device that can achieve a contrast ratio above 20 dB for an incident light power of 100 mW. This proposal is yet to be demonstrated in experiments.

In contrast to the work of Manipatruni *et al.*[29] where nonreciprocity is based on a nonlinear response of an optomechanical system, Hafezi and Rabl[30] proposed another optomechanical approach which can lead to nonreciprocal behavior even at single photon level. The proposal relies on enhanced nonlinear coupling between a mechanical mode of a WGM microring resonator and an optical mode with a probe light traveling in the same direction as the strong pump field. This leads to different transmission properties for the probe light fields traveling in the same or opposite directions. The light in the direction of the pump field is transmitted whereas that in the opposite direction is blocked by the resonator. This proposal has not been realized yet.

In 2009, Yu and Fan[31] proposed to use interband transitions induced by spatio-temporal refractive-index modulations in photonic structures for nonreciprocal behavior without magneto-optics. The nonreciprocal behavior relies on the shifts of the frequency and wavevector during the photonic transition. In a structure with modulated refractive index, the frequency ω_1 of the light in the forward direction is converted to a higher frequency $\omega_2 > \omega_1$; however, the light propagating in the backward direction is not affected by the modulation and stays intact. If an absorption filter that absorbs the light at ω_2 completely is placed at the output, the system will behave as an isolator which blocks the light in the forward direction but transmits it in the backward direction. An interesting property of this approach is that it is

a linear process and that the photonic transition does not depend on the phase or the amplitude of the incident light.

Although Yu and Fan[31] proposed to use a microring resonator for experimental realization, in 2012 Lira *et al.*[32] demonstrated their proposal and achieved nonreciprocity in a silicon slotted waveguide structure that was electrically driven to induce indirect interband photonic transition. Here, an indirect interband photonic transition took place between two optical modes having different longitudinal wave vectors, and transverse modal profiles with different symmetries. By applying an electrical modulation of 10 GHz, corresponding to the frequency difference between the optical modes of interest in their slotted waveguide, the authors achieved a contrast of 3 dB at an applied electrical signal power of 25 dBm. The insertion loss of the system was around 70 dB.

B11d. What makes our scheme different than above mentioned experimental realizations and what are the advantages? In our work, we used two directly coupled microtoroid resonators (quality factors of the order of 10^7) configured in an add-drop filter structure. One of the resonators is an active resonator with erbium ions as the embedded gain dopants within silica matrix whereas the other has passive silica loss at the λ=1.55μm band. Although the demonstrated nonreciprocity in our work also relies on nonlinearity, conceptually it is very different than the above works. The key point in our work is the use of PT-symmetric concept, where the loss in passive resonator is balanced with the gain in the active resonator and the coupling strength between the resonators is adjusted such that the system operates in the broken PT phase. As a result, in the broken PT-symmetry phase the optical field is strongly localized in the resonator with gain, which in turn enhances the nonlinear process (i.e., the nonlinearity can be observed with low power levels). In the unbroken phase there is no field localization and hence one needs higher power levels to observe the nonlinearity. This is seen clearly in Fig. S9 and Fig. 3a of the main text. There is a significant difference between the observed nonreciprocity in the broken- and unbroken-phases.

Up to date there was no reported experiment in the literature which utilizes PT-symmetric structures to achieve nonreciprocal light transmission. Our work is the first experimental demonstration bringing together the PT-symmetric concepts with nonlinearity to demonstrate nonreciprocal light transmission which is crucial for many optical devices and photonic applications. The advantages of our scheme, which brings together PT-symmetric concepts with nonlinearity-induced nonreciprocal light transmission, over the non-PT schemes

utilizing nonlinearity are significant reduction in the input power to observe nonreciprocity (~1μW in this work versus 3W in Ref. [18], 0.310W in Ref. [20] and ~ 85μW in Ref. [21]), higher contrast, smaller footprint and complete absence of the signal in one direction but resonantly enhanced transmission in the other direction. Unlike all the experimental works mentioned above (those utilizing magneto-optical effects, nonlinearity and interband transitions), we observed in this work a complete absence of resonance peak in one direction. Our work constitutes the first direct experimental proof of the connection between nonreciprocity and PT-symmetry which has been largely confused [see the work by Feng *et al.*[33] and comments on this article by Fan *et al.*[11], as well as the paper Wang *et al.*[34] and the comment by Petrov *et al.*[35]].

C. Imperfect gain/loss balance in PT-symmetric systems

In PT-symmetric systems, formed by coupled structures such as waveguides or resonators, with exactly balanced gain and loss, the phase transition (*PT-symmetry breaking*) from broken to unbroken symmetry is a sharp bifurcation in orthogonal directions in the real parts of the eigenfrequencies of the supermodes. This is accompanied by a sharp orthogonal coalescence of imaginary parts of the eigenfrequencies. However, in our experiments, we observed that the bifurcations were not so sharp and orthogonal as predicted by the theory of perfectly balanced systems, but rather there is a smooth gradual separation. We attributed this to the imperfection in gain/loss balance.

To explain this smooth bifurcation, we formulate a theoretical model in which the gain and loss are not perfectly balanced[36]. We construct the equations of motion of linearly coupled oscillators x and y,

$$\frac{d^2 x}{dt^2} + \mu \frac{dx}{dt} + \omega^2 x + \kappa y = 0$$

$$\frac{d^2 y}{dt^2} - \nu \frac{dy}{dt} + \omega^2 y + \kappa x = 0 \qquad (S.9)$$

Both oscillators have the same natural frequency ω, the parameters μ and ν are a measure of the loss and the gain, and κ is the coupling strength. We seek solutions of the form $e^{i\lambda t}$, which lead to the quartic polynomial equation

$$\lambda^4 - i(\mu-\nu)\lambda^3 - (2\omega^2 - \mu\nu)\lambda^2 + i\omega^2(\mu-\nu)\lambda - \kappa^2 + \omega^4 = 0 \tag{S.10}$$
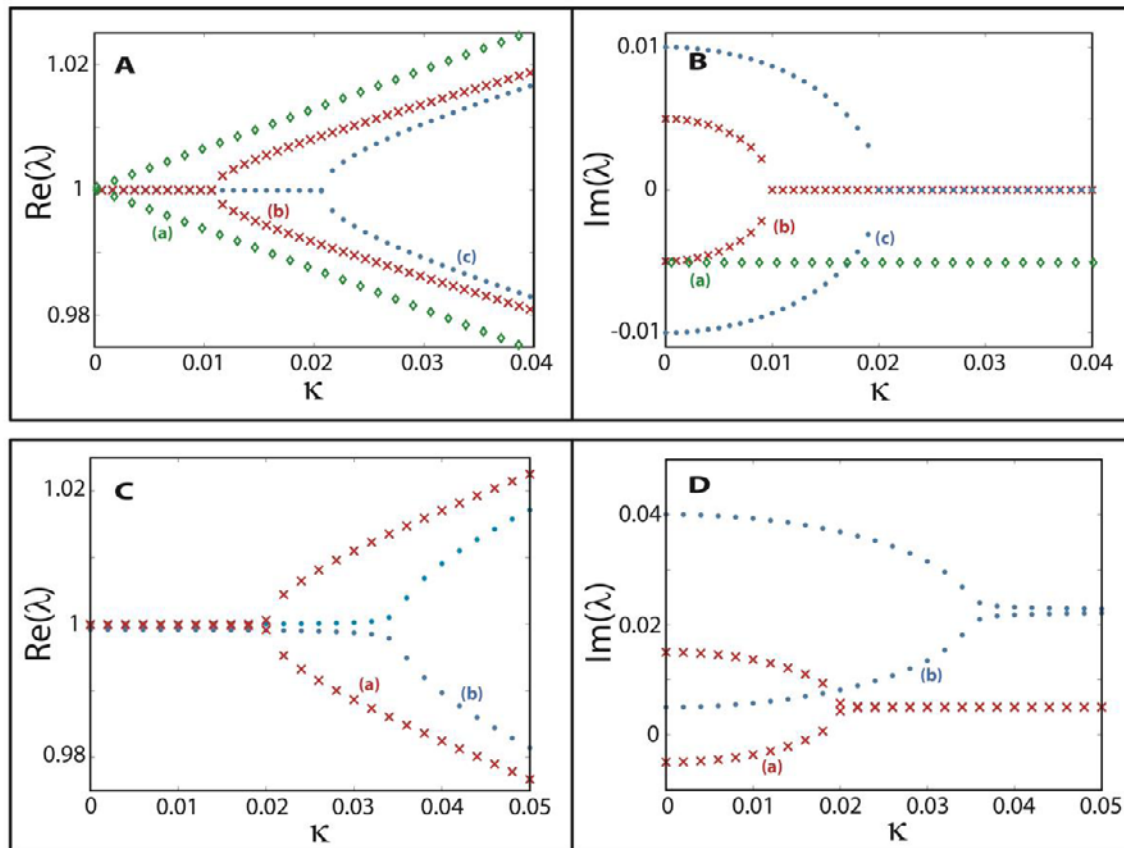

Fig.S13. Real and imaginary parts of the eigenfrequencies of the coupled system as a function of the coupling strength. The case where both of the oscillators are lossy $\mu = -\nu = 0.01$ is depicted in green diamond marks [A(a) and B(a)]. Exactly balanced gain and loss cases for small loss ($\mu = \nu = 0.01$) and larger loss ($\mu = \nu = 0.02$) are shown in [A(b) and B(b)]and [A(c) and B(c)], respectively, with brown crosses and blue solid circles. Real and imaginary parts of the eigenfrequencies for unbalanced loss and gain are given in (C) and (D), respectively. Loss and gain parameters are set as ($\mu = 3\nu = 0.03$) and ($\mu = 8\nu = 0.08$), respectively, for [C(a) and D(a)] brown cross marks and for [C(b) and D(b)] blue solid circle marks.

We have numerically solved this equation for $\omega = 1$ at various coupling strengths and gain-to-loss ratios. The real and imaginary parts of the eigenfrequencies of this coupled system are plotted in **Fig. S13** as functions of coupling strength κ and for chosen values of gain-to-loss ratios. We see that for the case of exactly balanced loss and gain, the bifurcation of the real and imaginary parts of the eigenfrequencies at the phase transition point is sharp and in orthogonal directions (**Figs. S13A** and **S13B**). However, for the unbalanced case the bifurcations are not abrupt, but rather are smooth (**Figs. S13C** and **S13D**). The degree of smoothness increases with increasing imbalance between gain and loss. Moreover, for the unbalanced loss-and-gain case the eigenfrequencies are never real and there is always a nonzero imaginary part.

It is also of critical importance to notice that for the special case in which the loss and gain are exactly balanced, the coupled equations of motion for $x(t)$ and $y(t)$ above can be derived from a Hamiltonian H,

$$H = pq + \gamma\left(yq - xp\right) + \left(\omega^2 - \gamma^2\right)xy + \frac{1}{2}\kappa\left(x^2 + y^2\right) \tag{S.11}$$

where p and q are momenta conjugate to x and y, and $2\gamma = \mu = \nu$. (The existence of a Hamiltonian is surprising because the system has loss and gain.) In this case, the energy H of the system is exactly conserved, although it is not a simple expression such as the sum of the squares of the momenta and the coordinates. Interestingly, if the coupling strength κ becomes strong enough, the frequencies become complex. Thus, there are two regions of broken PT symmetry, one for weak coupling and one for strong coupling[36]. Because the system is Hamiltonian, it can be quantized by imposing the requirement that x and p (and also y and q) obey equal-time commutation relations. One can then find the quantized energies of the Hamiltonian. One obtains the remarkable result that the quantum energies are real for exactly the same range of parameters that the classical frequencies are real; that is the region of unbroken PT symmetry. The quantum energies become complex when the classical frequencies are complex; that is in the region of broken PT symmetry[36].

Our experimental results depicted in Fig. 2 of the main text show the same behavior as the numerical results for our theoretical model shown in Fig. S13 C(a) and D(a), implying that the gain and loss in the experiments are not exactly balanced. In Figs. S13 A(a) and B(a), we see that for two coupled lossy oscillators (passive resonators), the difference of the real parts

of the eigenfrequencies increases with increasing coupling strength, whereas the imaginary parts remain equal. These numerical predictions agree well with the results of our experiments as shown in Figs. 2a and b of the main text; that is, the mode splitting (difference in the real parts of the eigenfrequencies) increases with increasing coupling strength while the difference in the imaginary parts of the eigenfrequencies stays the same. Finally, as depicted in Fig. 2c and d, we have observed in the experiments that the higher the initial loss (lower Q) of the resonators, the higher the coupling strength needed to observe the transition from broken-symmetry to unbroken-symmetry region. This is indeed what is found in the numerical solutions of the characteristic equation of the theoretical model (Fig. S13). Thus, the theoretical model introduced here and our experimental observations are consistent. Our model is physically realistic because in practical realizations it is almost impossible to have exactly balanced loss and gain.

The observation in our experiments and the theoretical model above is critical in two ways. First, imposing exactly balanced loss and gain in coupled systems for extended durations of time is not practical. Second, In the broken-symmetry phase, the field propagating in the PT-symmetric system is always confined in the structure with gain, thereby experiencing a strong overall gain and leading to enhanced transmission. At the phase transition point, the change in the gain experienced by the field should be abrupt in the ideally balanced gain and loss situation. Thus, if the coupling strength is changed by a very small amount around the phase transition point, there is a large abrupt change in the real and imaginary parts of the eigenfrequencies, leading to an abrupt change in the amplification or the gain experienced by the field. In the non-ideal case where the bifurcation is not orthogonal but smoothened, the change in the gain/amplification experienced by the field around the phase transition point is reduced.

Finally, we should note here that the smooth bifurcation issue was also discussed by Benisty *et al.*[37] from a different perspective: They attributed the smoothness around the phase transition point to a complex coupling arising as the gain is tuned in one of the systems.

References:

1. Armani, D. K., Kippenberg, T. J., Spillane, S. M., Vahala, K. J. Ultra-high-Q toroid microcavity on a chip. *Nature* **421**, 925-928 (2003).

2. Yang, L., Carmon, T., Min, B., Spillane, S. M., Vahala, K. J. Erbium-doped and Raman microlasers on a silicon chip fabricated by the sol-gel process. *App. Phy. Lett.* **86**, 091114 (2005).

3. He, L., Ozdemir, S. K., Yang, L. Whispering gallery microcavity lasers. *Laser & Photon.Rev.* **7**, 60-82 (2013).

4. He, L., Ozdemir, S. K., Xiao, Y. F., Yang, L. Gain-induced evolution of mode splitting spectra in a high-Q active microresonator. *IEEE J. Quantum Electron.* **46**, 1626-1633 (2010).

5. He, L., Ozdemir, S. K., Zhu, J., Yang, L. Ultrasensitive detection of mode splitting in active optical microcavities. *Phys. Rev. A* **82**, 053810 (2010).

6. Peng, B., Ozdemir, S. K., Zhu, J., Yang, L. Photonic molecules formed by coupled hybrid resonators, *Opt. Lett.* **37**, 3435-3437 (2012).

7. Anetsberger , G. *et al.* Near-field cavity optomechanics with nanomechanical oscillators. *Nat. Phys.* **5**, 909-914 (2009).

8. Monifi, F., Friedlein, J., Ozdemir, S. K., Yang, L. A robust and tunable add-drop filter using whispering gallery mode microtoroid resonator. *J. Lightw. Technol.* **30**, 3306-3315 (2012).

9. Gorodetsky, M. L., Ilchenko, V. S. Optical microsphere resonators: optimal coupling to high-Q whispering-gallery modes. J. Opt. Soc. Am. B. 16, 147-154 (1999).

10. Haus, H. A. *et al.* Optical resonators and filters. in *Optical Microcavities* Edited by Vahala. K. (World Scientific Publishing Co. Pte. Ltd) 1-37 (2004).

11. Fan, S. et al. Comment on "Nonreciprocal Light Propagation in a Silicon Photonic Circuit" *Science* **335**, 38 (2012).

12. Jalas, D. et al. What is- and what is not- an optical isolator. *Nat. Photon.* **7**, 579-582 (2013).

13. Krause, M., Renner, H., Brinkmeyer, E. *Electron. Lett.* **44**, 691-693 (2008).

14. Luo, Z., Ye, W., Yuan, X., Zhu, Z., Zeng, C., Ji, J. Complete optical on-chip isolation based on asymmetric stimulated Raman gain/loss. Opt. Lett. **37**, 674-676 (2012).

15. Huang, X., Fan, S. Complete all-optical silica fiber isolator via Stimulated Brillouin Scattering. *J. Lightwave Technol*. **29**, 2267–2275 (2011).

16. Poulton, C. G., Pant, R., Byrnes, A., Fan, S., Steel, M. J., Eggleton, B. J. Design for broadband on-chip isolator using stimulated Brillouin scattering in dispersion-engineered chalcogenide waveguides. Opt. Exp. **20**, 21235-21246 (2012).

17. Gallo, K., Assanto, G. All-optical diode based on second-harmonic generation in an asymmetric waveguide. *J. Opt. Soc. Am. B*. **16**, 267–269 (1999).

18. Gallo, K., Assanto, G., Parameswaran, K. R., Fejer, M. M. All-optical diode in a periodically poled lithium niobate waveguide. *Appl. Phys. Lett*. **79**, 314–316 (2001).

19. Tocci, M. D., Bloemer, M. J., Scalora, M., Dowling, J. P., Bowden, C. M. Thin film nonlinear optical diode. *Appl. Phys. Lett*. **66**, 2324–2326 (1995).

20. Kang, M. S., Butsch A., Russell, P. St. J. Reconfigurable light-driven opto-acoustic isolators in photonic crystal fibre. *Nature Photon*. **5**, 549-553 (2011).

21. Fan, L. *et al*. An all-silicon passive optical diode. *Science* **335,** 447-450 (2012).

22. Bi, L. *et al*. On-Chip Optical Isolation in Monolithically Integrated Non-Reciprocal Optical Resonators. *Nature Photon*. **5**, 758-762 (2011).

23. Tien, M.-C., Mizumoto, T., Pintus, P., Kromer, H., Bowers, J. E. Silicon ring isolators with bonded nonreciprocal magneto-optic garnets. *Opt. Express*. **19**, 11740 (2011).

24. Yokoi, H., Mizumoto, T., Shoji, Y. Optical nonreciprocal devices with a silicon guiding layer fabricated by wafer bonding. *Appl. Opt*. **42**, 6605–6612 (2003).

25. Sung, S. Y., Qi, X., Stadler, B. J. H. Integrating yttrium iron garnet onto nongarnet substrates with faster deposition rates and high reliability. *Appl. Phys. Lett*. **87**, 121111 (2005).

26. Ghosh, S. *et al*. Adhesively bonded Ce:YIG/SOI integrated optical circulator. *Opt. Lett*. **38**, 965-967 (2013).

27. Kono, N., Kakihara, K., Saitoh, K., Koshiba, M. Nonreciprocal microresonators for the miniaturization of optical waveguide isolators. *Opt. Express*. **15**, 7737–7751 (2007).

28. Wang, Z., Fan, S. Optical circulators in two-dimensional magneto-optical photonic crystals. *Opt. Lett*. **30**, 1989–1991 (2005).

29. Manipatruni, S., Robinson, J., Lipson, M. Optical nonreciprocity in optomechanical structures. *Phys. Rev. Lett.* **102**, 213903 (2009).

30. Hafezi, M., Rabl, P. Optomechanically induced non-reciprocity in microring resonators. *Opt. Express.* **20**, 7672–7684 (2012).

31. Yu, Z. & Fan, S. Complete optical isolation created by indirect interband photonic transitions. *Nature Photon.* **3**, 91–94 (2009).

32. Lira, H., Yu, Z., Fan, S., Lipson, M. Electrically driven nonreciprocity induced by interband photonic transition on a silicon chip. *Phys. Rev. Lett.* **109**, 033901 (2012).

33. Feng, L. *et al.* Nonreciprocal light propagation in a silicon photonic circuit. *Science* **333**, 729-733 (2011).

34. Wang, C., Zhong, X.-L. & Li, Z.-Y. Linear and passive silicon optical isolator. *Sci. Rep.* **2**, 674 (2012).

35. Petrov, A. *et al.* Comment on "Linear and passive silicon optical isolator" in Scientific Reports 2, 674 (2012).

36. Bender, C. M., Gianfreda, M., Ozdemir, S. K., Peng, B, Yang, L. Twofold Transition in PT-Symmetric Coupled Oscillators. Phys. Rev. A. **88**, 062111 (2013).

37. Benisty, H., Yan, C., Degiron, A., Lupu, A. T. Healing near-PT-symmetric structures to restore their characteristic singularities: Analysis and examples. *J. Lightw. Technol.* **30**, 2675-2683 (2012).